Science of the Total Environment 900 (2023) 165856

Contents lists available at ScienceDirect

Science of the Total Environment

journal homepage: www.elsevier.com/locate/scitotenv

The non-coevolution of DIC and alkalinity and the CO_2 degassing in a karst river affected by acid mine drainage in Southwest China

Qingguang Li [a,b], Pan Wu [a,*], Shilu Wang [b], Jiangxun Huang [a], Weiqi Lu [b], Di Tan [b], Shangyi Gu [a], Bailing Fan [c]

[a] College of Resources and Environmental Engineering, Key Laboratory of Karst Georesources and Environment, Ministry of Education, Guizhou University, Guiyang 550025, China
[b] State Key Laboratory of Environmental Geochemistry, Institute of Geochemistry, Chinese Academy of Sciences, Guiyang 550081, China
[c] College of Eco-Environmental Engineering, Guizhou Minzu University, Guiyang 550025, China

ARTICLE INFO

Editor: Christian Herrera

Keywords:
Non-coevolution of DIC and alkalinity
Acidified mine drainage
DIC transport processes
HCO_3^--neutralized degassing
Proton-enhanced degassing
Degassing scale

ABSTRACT

Dissolved inorganic carbon (DIC) in mine water generated during coal mining is a large and potential source of atmospheric CO_2, however its geochemical behaviors under the influence of AMD in relation to CO_2 degassing and carbonate buffering are not well known. In this study, water temperature, pH, DO, alkalinity, Ca^{2+} concentration, and the carbon isotope of DIC were measured monthly from November 2020 to November 2021 and carbonate chemistry and CO_2 emission flux were calculated to reveal the processes of DIC evolution and CO_2 degassing from the Chetian River draining a karst region, which is materially affected by the input of large quantities of AMD. The results showed that carbonate erosion, the mineralization of terrestrial organic matter, and domestic sewage input are all identified to contribute DIC to different degrees to the river. Throughout the year, the Chetian River undergoes high-intensity CO_2 degassing, which is dominated by HCO_3^--neutralized degassing and proton-enhanced degassing in different reaches. The pCO_2 in the river under the influence of AMD is as high as 237,482 μatm, while the F-CO_2 approaches 316.9 g C m^{-2} d^{-1}. Meanwhile, the carbonate system in the downstream karst river buffers an average of 85.2 % of DIC release at the river's outlet. The input of AMD significantly altered the carbon cycle of the surface watershed in the headwaters of tributaries, and greatly enhanced the release of CO_2 from surface water to the atmosphere; meanwhile, the buffering of carbonates on acidity in the water of main streams causes pCO_2 to rapidly reduce over a short distance. Obviously, the carbon emission effect generated by the interaction between AMD and carbonate mainly occurs in the tributary water system. Considering the huge amount of AMD worldwide, this large potential source of atmospheric CO_2 requires a specific and precise quantitative analysis based on actual observations.

1. Introduction

As a result of coal development in China, the total amount of mine water discharged annually has reached 6.0–8.0 billion m^3 (Sun et al., 2012, 2020; Feng et al., 2014; Wu, 2014; Gu et al., 2021). To date, researchers have focused primarily on the sources and quality of mine water from the perspective of coal mine safety and resource utilization (Wu, 2014; Balci and Demirel, 2018; Chen et al., 2021; Li et al., 2021; Vöröš et al., 2021). In practical terms, mine water, especially acidified mine drainage (AMD), may constitute a long-neglected source of CO_2 in the atmosphere. During the process of pressure-relief mining, the partial pressure of CO_2 (pCO_2) in original formation water rich in dissolved inorganic carbon (DIC) can exceed the atmospheric background pCO_2, leading to the release of a large amount of CO_2 into the atmosphere. In reality, the measured DIC content in formation water in coal-bearing strata is generally high due to the mineralization of coal organic matter during coal formation, added to the dissolution of the CO_2 generated by this process (McIntosh et al., 2002; Golding et al., 2013). The DIC content in formation water in the San Juan Basin has been reportedly reached 14,701 mg/L (Lemay, 2003), while the reported DIC in the Huaibei Coalfield of China was up to 5400 mg/L (Li et al., 2016).

Coal mining exposes and oxidizes sulfides, such as pyrite, leading to the acidification of mine drainage (Singer and Stumm, 1970; Rice and Herman, 2012; Tao et al., 2012; Strosnider et al., 2014; Zhang et al.,

* Corresponding author.
E-mail address: pwu@gzu.edu.cn (P. Wu).

https://doi.org/10.1016/j.scitotenv.2023.165856
Received 25 May 2023; Received in revised form 22 July 2023; Accepted 26 July 2023
Available online 28 July 2023

2021). Water acidification significantly changes hydrochemical parameters, including pH, Eh, EC, and dissolved oxygen (DO) (Sasowsky and White, 1993; Nordstrom et al., 2015; Grande et al., 2016; Zhang et al., 2021), and can also affect CO_2 degassing and DIC carbon isotope evolution. Hercod et al. (1998) suggested that the oxidation of pyrite can generate sulfuric acid, consequently driving the conversion of nearly half of the DIC in the surface drainage into CO_2, which is subsequently released into the atmosphere. According to Fonyuy and Atekwana (2008), the $\delta^{13}C$-DIC of surface rivers affected by AMD becomes 1.0 ‰–3.0 ‰ heavier as a result of CO_2 degassing, and 50 %–98 % of DIC in surface water is released into the atmosphere through this process. In a study that examined the long-term influence of AMD on the CO_2 release at the whole-basin scale in the Susquehanna River, Raymond and Oh (2009) found that up to 3.10 Tg of carbon had been lost into the atmosphere over the last century in the watershed.

The effects of AMD input can cause DIC evolution and CO_2 degassing in karst freshwater watershed systems to become increasingly complex. In addition to changing the water's pH, the inflow of AMD disrupts the dissolution-precipitation balance of carbonates in freshwater. Over the past decade, the carbon sink effect of karstification has attracted widespread scholarly attention (Liu et al., 2011; Wang et al., 2015; Zeng et al., 2016; Huang and Li, 2019; Wang et al., 2019). However, when AMD encounters carbonate strata, it erodes the carbonate minerals and carries geological “old carbon” to the surface, increasing the carbon cycle load in the surface layers (Kruse and Strosnider, 2015). Considering the enormous amount of mine water that coal mining generates, the carbon cycle of AMD-driven karstification demands special attention.

Guizhou is a highly productive coal base in Southwest China. The high pyrite content in raw coal is a key factor in the massive production of AMD in this area (Feng et al., 2014; Tang et al., 2020; Liu et al., 2021). In addition, this area features widely distributed carbonate strata and well-developed karstification. These factors make the location ideal for studying the dynamic characteristics of CO_2 degassing and carbon emission scale associated with mine water acidification. As above-mentioned, when AMD enters surface water bodies with high DIC content, H^+ drives DIC to convert into CO_2, greatly promoting the release of CO_2 from surface water to the atmosphere; conversely, the buffering effect produced by the reaction of H^+ with carbonate rocks can increase the pH of water, thus inhibiting the release of CO_2. The overall impact of AMD on CO_2 release from surface water is determined by the coupling effect of the two processes mentioned above. However, the interaction mechanism between these two processes is still unclear, which hinders the scientific evaluation of AMD's carbon emission effect. Accordingly, the Chetian River, a tributary of the Huatan River in Jinsha County, Guizhou Province, was chosen as the subject of this study. The study sought to clarify the primary hydrochemical processes affecting the evolution of DIC and the characteristics of CO_2 degassing in surface water under the condition of AMD merging into superimposed karstification. An accurate evaluation of the scale of CO_2 degassing in the Chetian River driven by AMD was also anticipated.

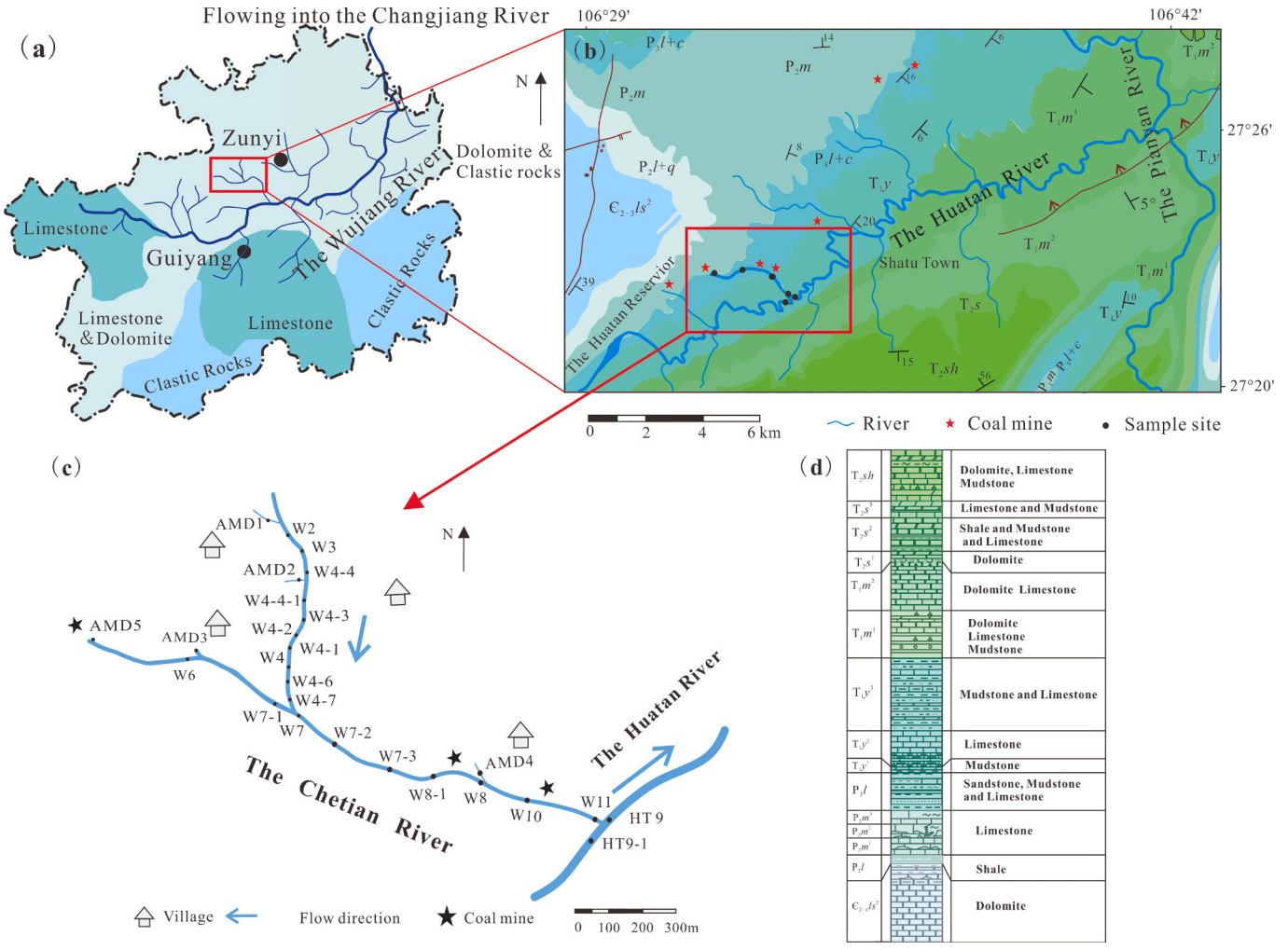

Fig. 1. (a) The location of the research area in Guizhou Province; (b) the geological background, river, and coal mine distribution within the study area; (c) sampling points arranged along the river; (d) regional geological histogram.

2. Materials and methods

2.1. Study area

The Chetian River (106°29′10″-106°42′24″E and 27°20′43″-27°26′4″N) is a primary tributary of the Huatan River (Fig. 1) that is severely affected by the input of AMD generated during coal mining. The Huatan River has a basin area of 321km^2 and a length of 59 km, and it flows from west to east and enters the Pianyan River, a tributary of the Wujiang River, and finally discharge into the Changjiang River. The historical maximum peak flow is 184.33m^3/s, and the annual average runoff is 130 million m^3. The basin is located in Northern Guizhou Province, Southwestern China, where karst landforms such as funnels, peak clusters, depressions, water holes, furrows, and natural bridges are widely distributed. The study area has a subtropical monsoon humid climate zone with an altitude of 760 m–1095 m and an annual average rainfall of 1057 mm.

The region is located in the north Guizhou platform uplift of the Yangtze platform. The outcrops in the study area are primarily Permian and Triassic strata (Fig. 1). Among these outcrops, the Longtan Formation (P_3l) is a coal-bearing rock series with a thickness of 95-110 m that is in pseudo-conformable contact with the Maokou Formation (P_1m) below and contains 4–8 layers of coal, 3 layers (C5, C8, C12) of which can be mined. The coal is anthracite with a medium sulfur content and high calorific value. In addition, a pyritic bedded deposit, which is patchy, nodular, and scattered within the clay rock, occurs at the bottom of the Longtan Formation and above the Maokou Formation in stratified and lamellar form. There are a series of coal mines distributed along the strike direction of the coal-bearing strata.

2.2. Sample collection

In this study, 24 sampling sites were set up in the Chetian River (Fig. 1), 5 of which are AMD outlets. Two sampling points, HT9 and HT9-1, are distributed before and after the confluence of the Chetian and Huatan rivers. In addition, 2 sets of atmospheric precipitation samples were collected in June and August 2021. Water samples for hydrochemical analysis were collected monthly from November 2020 to November 2021. During each sampling period, pH, water temperature (T/°C), DO, EC, and Eh were recorded using a YSI Pro Plus multiparameter water quality analyzer. The instrument's electrodes were calibrated the night before each sampling.

The samples for DIC carbon isotope analysis were filtered via a disposable syringe through a 0.45 μm nylon membrane filter with positive pressure and stored in 50 mL brown glass bottles. This operation sought to prevent the CO_2 in the water from being released during suction filtration. Notably, no bubbles remained in the container before sealing. The samples used for the anion and cation analysis were also filtered using the same method and stored in a 50 mL centrifuge tube; The samples for the cation analysis were added with nitric acid (Guaranteed Reagent) to adjust the pH < 2.0, while the samples for the anion analysis were stored without adding reagents. All samples were placed in a refrigerator at 4 °C for not >2 weeks.

2.3. Analysis

The field titration of alkalinity was carried out using a Merck alkalinity test (art. No. 1.11109.0001), and the error for 3 titrations was not >0.05 mmol/L. SO_4^{2-} was identified with an ICS-90 ion chromatograph produced by Dionex, Inc., USA; the test accuracy was ±5 %. The concentration of Ca^{2+} was determined by a Vista MPX inductively coupled plasma optical emission spectrometer (ICP-OES) produced by Varian, Inc., USA, with a measurement accuracy of better than ±5 %. Blank samples, parallel samples, and standard samples were added for data quality control.

A DIC carbon isotope analysis was performed using a continuous flow isotope ratio mass spectrometry (CF-IRMS, DELTA V Advantage gas isotope mass spectrometer equipped with a Gasbench). First, 0.2 mL of high-purity phosphoric acid was added to a high-borosilicate glass bottle. Next, the glass bottle was purged with high-purity helium gas for 7 min. Then, 0.5 mL of water was injected with a disposable syringe. After reaching equilibrium for 2 h, CO_2 was carried by the helium gas into the DELTA V Advantage for isotope analysis. The testing process employed interspersed parallel samples and international standard samples (NBS18 and IAEA-603) for quality control. The carbon isotope of DIC was expressed by δ^{13}C-DIC (‰) using the international standard sample VPDB as the standard. The calculation is shown in Eq. (1):

$$\delta^{13}C-DIC\ (‰) = \left[\left(R_{Sample} - R_{VPDB}\right)/R_{VPDB}\right] \times 1000‰ \quad (1)$$

2.4. Calculation of the concentrations of different DIC components

The dissociation constants for carbonic acid are functions of temperature and salinity (Millero, 2010). Consequently, the concentrations of different DIC components are actually functions of pH (Eqs. (2) to (4); Wolf-Gladrow et al., 2007). In this study, the concentrations of different DIC components were obtained using a theoretical calculation based on Eq. (5).

$$\gamma_0 = [H^+]^2/\left(K_1K_2 + K_1[H^+] + [H^+]^2\right) \quad (2)$$

$$\gamma_1 = K_1[H^+]/\left(K_1K_2 + K_1[H^+] + [H^+]^2\right) \quad (3)$$

$$\gamma_2 = K_1K_2/\left(K_1K_2 + K_1[H^+] + [H^+]^2\right) \quad (4)$$

$$TA = DIC \times (\gamma_1 + 2\gamma_2) + K_W/[H^+] - [H^+] \quad (5)$$

where K_W is the hydrolysis equilibrium constant; K_1 and K_2 are the first and second dissociation constants of carbonic acid, respectively; γ_0, γ_1, and γ_2 are the proportions of H_2CO_3*, HCO_3, and CO_3^{2-} in DIC, respectively; and TA represents the measured alkalinity.

The variation characteristics of different DIC components under AMD-driving conditions were revealed by calculating the carbon isotopic compositions of HCO_3^-, CO_2, and CO_3^{2-} at all sampling points according to the isotope mass balance (Eqs. (6) and (7); Mook et al., 1974; Samanta et al., 2015; Wang et al., 2019).

$$\delta^{13}C_{CO_2} = \delta^{13}C_{DIC} + 23.644 - 9701.5/T \quad (6)$$

$$\Delta_{HCO_3^- - CO_2} = -9.866 \times \frac{10^3}{T} + 24.12 = \delta^{13}C_{HCO_3^-} - \delta^{13}C_{CO_2} \quad (7)$$

3. Results

3.1. Hydrochemical parameters

3.1.1. pH

The pH at sampling site W2, the headwater of the upper reaches of the Chetian River, was relatively stable throughout the year, varying from 7.16 to 7.60, with an average value of 7.36 ± 0.17. AMD4 was a sampling point for AMD outflow year-round; the pH of this point also remained stable throughout the year, varying from 2.29 to 2.99, with an average of 2.69 ± 0.18. Meanwhile, AMD3 represented a perennial artesian fountain that overflowed from coal-bearing strata; here, the pH gradually rose from 4.01 to 5.20 during the sampling period. The spatial variations of pH displayed a remarkable decline at sites W4-4-1, W7-1, and W10 as the AMD from sites AMD2, AMD3, and AMD4 flowed into the river. Meanwhile, pH demonstrated a marked increase at sites W8-1 and HT9.

3.1.2. Water temperature

In summer (June to August 2021), the water temperature of the Chetian River varied from 19.2 °C to 29.4 °C, with an average of 21.6 ±

1.79 °C. In contrast, January 2021, which represented a winter measurement, was the coldest month during the entire sampling period, with an average temperature of 12.5 ± 2.47 °C (Table S1; Fig. S1).

3.1.3. DO

In winter, the content of DO varied from 2.72 mg/L to 7.16 mg/L, with an average of 4.58 ± 1.48 mg/L, which was higher than the average level of 3.36 ± 1.37 mg/L during autumn. The level of DO was significantly lower in the waters from W4-4-1 to W8-1, which were affected by AMD than that from the section unaffected by AMD (Fig. S2). The level of DO at site AMD3 was stable at a relatively low value, varying in the range of 0.61–1.08 mg/L, with an average of 0.94 mg/L.

3.2. DIC concentration and carbon isotope

3.2.1. DIC components

The DIC in the Chetian River presented a gradually decreasing trend as the water flowed downstream (Fig. 2). The annual variation of DIC at W4-4-1 ranged from 240.0 mg/L to 617.8 mg/L, with an average of 401.0 ± 127.9 mg/L, which was the highest content of DIC among all sampling points. In contrast, the DIC concentration at sampling site W11 varied from 46.2 to 213.9 mg/L, with an average of 93.4 ± 43.7 mg/L. The DIC content at this point was the lowest in the Chetian River.

3.2.2. δ^{13}C-DIC

The δ^{13}C-DIC of W2, W3, and W4 located in the upstream segment was higher in winter and spring than in summer and autumn. Conversely, the segments from W4-4-1 to W8 showed higher values in summer and autumn than in winter and spring. The δ^{13}C-DIC rapidly decreased in the downstream segment of W10 to W11. The annual average of δ^{13}C-DIC at the confluence point with the Huatan River (HT9) was −10.2 ‰, while the largest variation of δ^{13}C-DIC in the river segment from W2 to W11 ranged from −4.0 ‰ to −9.9 ‰ in November 2021. When AMD was added at AMD2 and AMD4, δ^{13}C-HCO_3^- and δ^{13}C-CO_2 increased significantly (Fig. 3).

3.3. pCO_2 and CO_2 fluxes

The pCO_2 is assumed to be in equilibrium with the sampled waters and calculated via the following equation (Eq. (8); Cai and Wang, 1998; Cai et al., 2008):

$$pCO_2 = [CO_2]/K_H = C_T \times [H^+]^2 / \left[\left([H^+]^2 + [H^+]\, K_1 + K_1 \times K_2 \right) \times K_H \right] \quad (8)$$

where K_1 and K_2 are the temperature-dependent first and second dissociation constants, respectively; K_H is the Henry's Law constant; and C_T is the concentration of DIC. The revised equations of pK_1 and pK_2 for salinities can be obtained from Cai and Wang (1998).

The CO_2 flux (F-CO_2) across the water–air interface is calculated based on the stagnant-layer model (Eq. (9); Cai and Wang, 1998):

$$F - CO_2 = K_T \times K_H \times \left(pCO_{2(water)} - pCO_{2(air)} \right) \quad (9)$$

where $pCO_{2(water)}$ represents the partial pressure of CO_2 in the water near the interface and $pCO_{2(air)}$ is set as 360 μatm; K_T and K_H are the gas transfer velocity (m d^{-1}) and Henry's constant, respectively (Cai and Wang, 1998). Clark et al. (1994) proposed a mean gas transfer rate of 1.06 m d^{-1}, while Alin et al. (2011) and Zhang et al. (2019) believed that the factor k could be 60 % greater in streams and small rivers < 100 m wide than in rivers with channels > 100 m. In this study, the relationship between a gas transfer velocity of CO_2 (K_T) and steady wind speed 10 m above the river (u), and the temperature-dependent Schmidt number (*Sc*) is as shown in Eq. (10) (Wanninkhof, 1992, 2014; Tan et al., 2021):

$$K_T = \left[2.5 \times \left(0.5246 + 1.6256 \times 10^{-2} t + 4.9946 \times 10^{-4} t^2 \right) + 0.3u^2 \right] (Sc/660)^{-1/2} \quad (10)$$

In the Chetian River, the pCO_2 significantly decreased along the flow

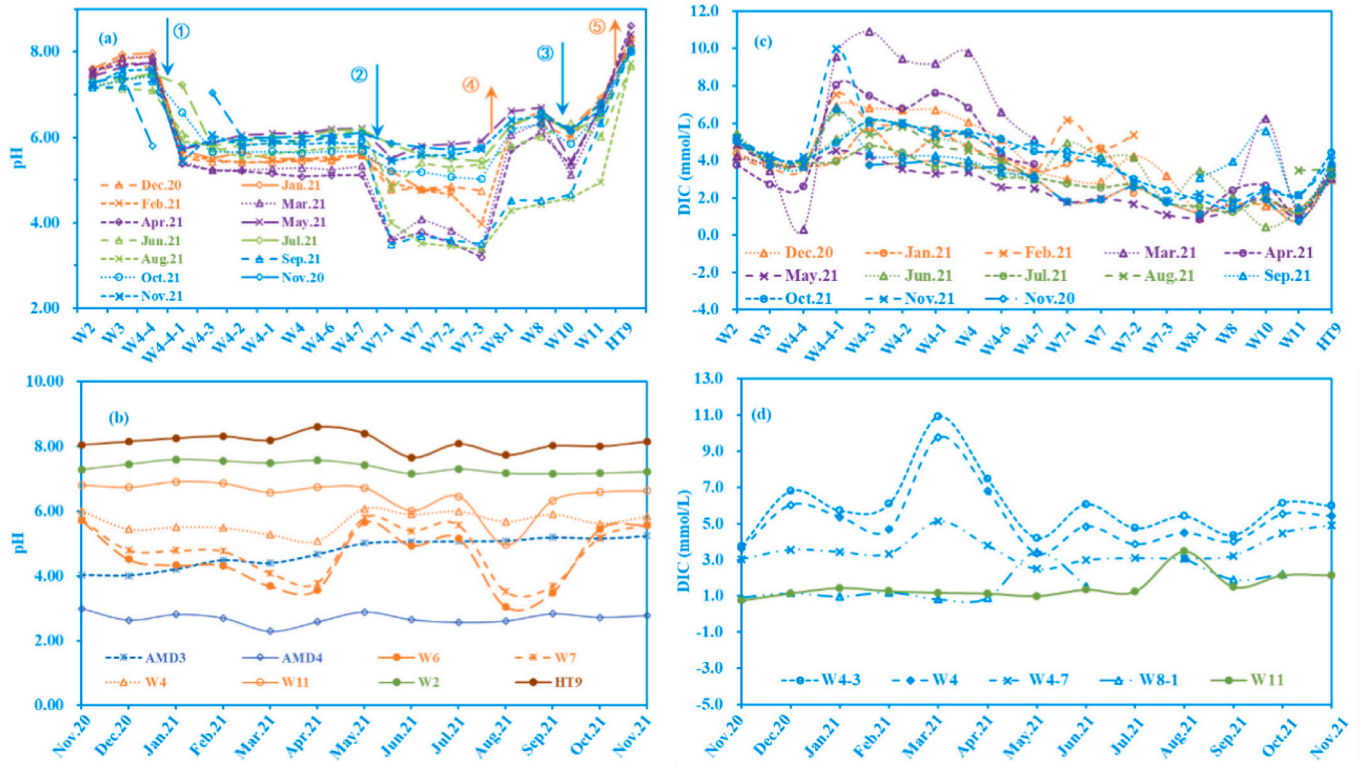

Fig. 2. The spatial variations of water pH (a) and DIC concentrations (b) along the water flow of Chetian River in the different month. And the monthly variation of pH (c) and DIC concentration (d) in water at some key sampling sites.

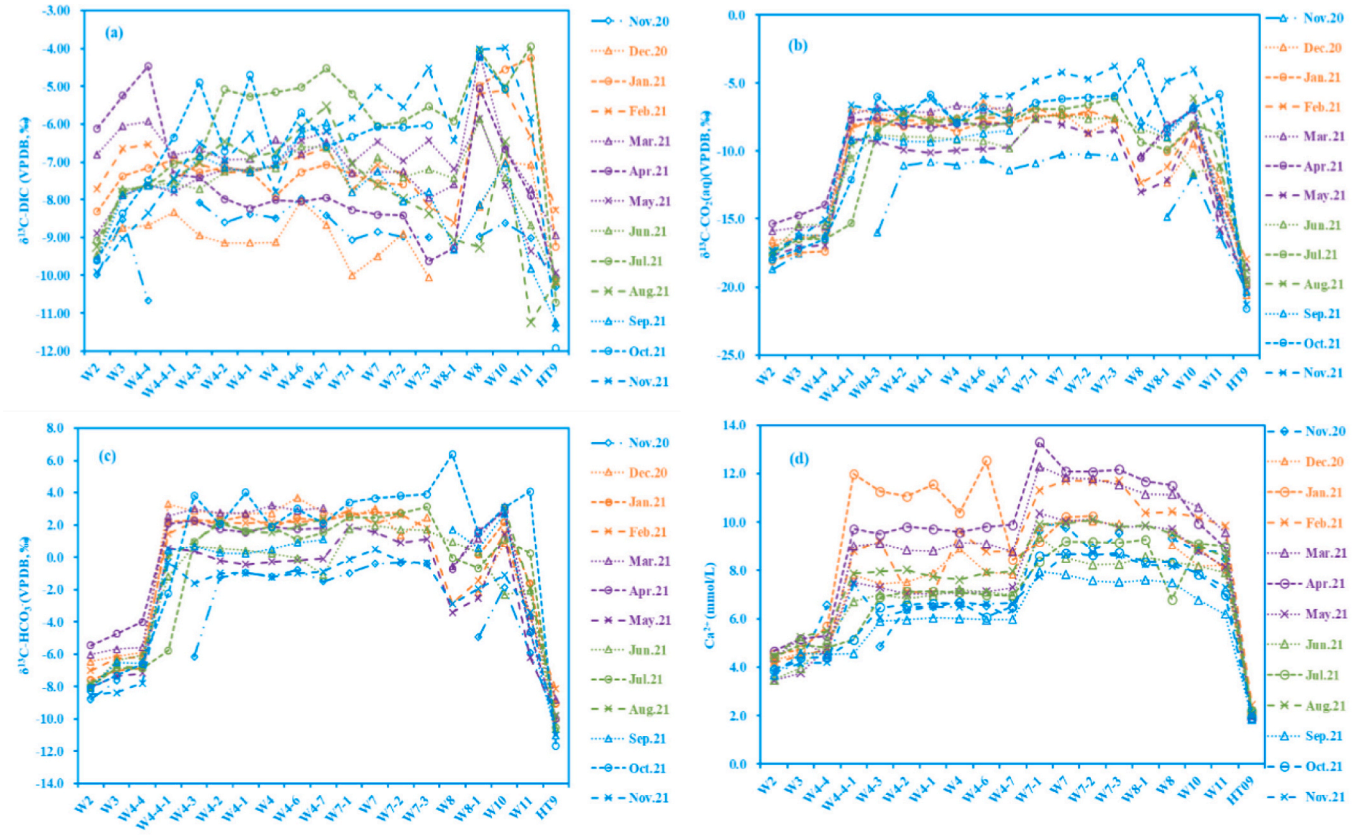

Fig. 3. Spatial and temporal variation characteristics of (a) δ^{13}C-DIC, (b) δ^{13}C-HCO_3^-, (c) δ^{13}C-CO_2, and (d) Ca^{2+} content in the Chetian River Basin.

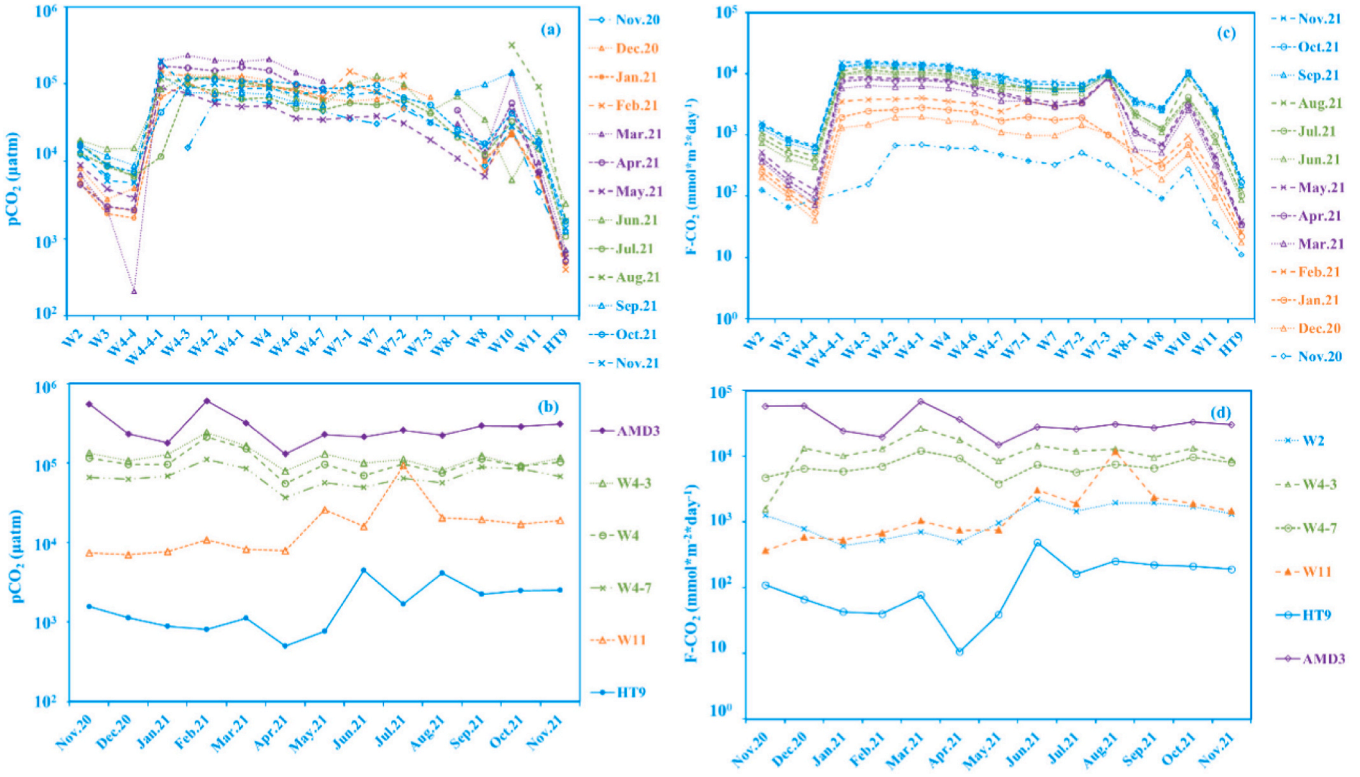

Fig. 4. (a) Temporal and spatial variation of pCO_2 in the Chetian River Basin; (b) annual variation characteristics of pCO_2 at sampling points AMD3, W4-3, W4, W4-7, W11, and HT9; (c) spatial and temporal variation of F-CO_2 in the Chetian River Basin; (d) annual variation of F-CO_2 at sampling points AMD3, W2, W4-3, W4-7, W11, and HT9.

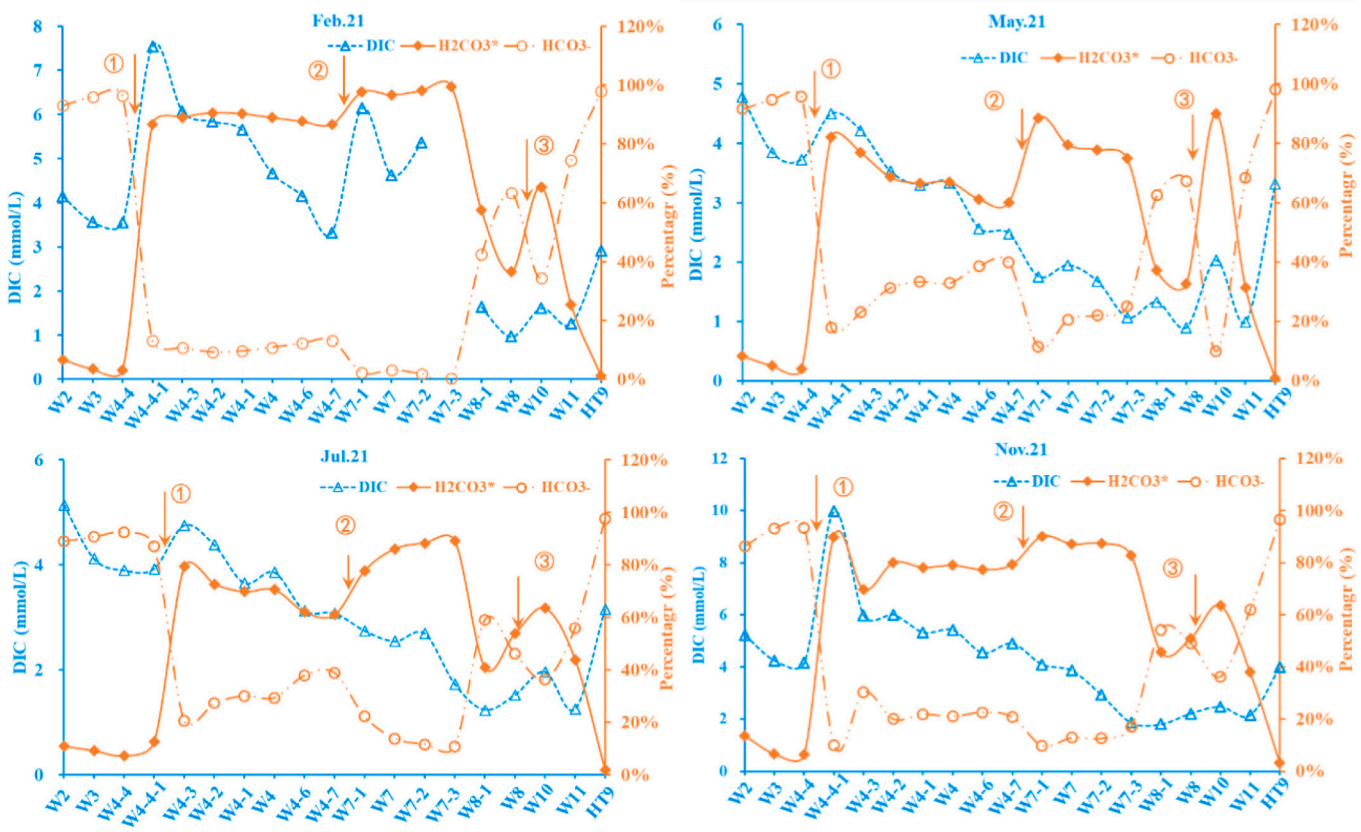

Fig. 5. Variation characteristics of DIC components in the Chetian River Basin in different seasons.

direction from an average of 116,308 μatm at W4-4-1 to 17,734 μatm at W11 during this study, suggesting strong CO_2 degassing characteristics (Fig. 4; Table S2). In March 2021, this value decreased from 37,482 μatm to 9695 μatm. At the confluence of the Chetian and Huatan rivers (HT9), the average pCO_2 was 1068 μatm, which was far lower than the pCO_2 in the Chetian River.

4. Discussion

4.1. pH drives dynamic transformation of different DIC components

The oxidation of pyrite and other sulfides is a principal cause of water acidification during coal mining (Pope et al., 2010; Weisener and Weber, 2010; Sağlam et al., 2016), thus affecting the dynamic balance of different DIC components in the water and the CO_2 transport process at the water-air interface. In the study area, the pH of AMD was found to fall as low as 2.29 in observations that emerged from the current study. In winter, the rainfall is relatively scarce in the study area, and the main replenishment source comes from AMD generated during coal mining, causing the river's pH to be relatively low (W4-4-1 to W8-1; Fig. 2). In contrast, a large amount of precipitation has a diluting effect in the rainy season, resulting in a rise in pH in the Chetian River. When the Chetian River flowed through W8-1, the water was in direct contact with limestone, allowing the dissolution of carbonate to buffer the acidity in the water. At HT9, the water of the Chetian River was diluted by the Huatan River, which had a larger discharge, initiating a rapid rise in pH.

Fig. 5 shows variations in pH drove the dynamic transformation of the HCO_3^- and H_2CO_3* components (Eqs. (11) and (12)), reflecting the influence of AMD inflow (Li and Wu, 2022). This relationship is also verified in Fig. S3. As the pH decreased, the water alkalinity and HCO_3^- concentration gradually decreased, while the CO_2 content gradually increased. Notably, the concentration relationship of each component is calculated according to the proportional relationship of DIC species under different pH conditions. The actual water-soluble CO_2 concentration under low pH conditions is usually lower than the calculated result (Vesper and Edenborn, 2012; Vesper et al., 2016).

$$pH = pK_1 - Log[H_2CO_3^*] + Log[HCO_3^-] \ (pH < 8.33) \quad (11)$$

$$pH = pK_2 - Log[HCO_3^-] + Log[CO_3^{2-}] \ (pH > 8.33) \quad (12)$$

As shown in Fig. 6, the $\delta^{13}C$-HCO_3^- and $\delta^{13}C$-CO_2 increased by 10.5 ‰ and 11.0 ‰, respectively, as the pH decreased from 8.5 to 4.5, indicating that obvious isotopic fractionation occurred during CO_2 degassing. As the HCO_3^- concentration decreased, the $\delta^{13}C$-HCO_3^- gradually stabilized at +2.3 ‰, while the $\delta^{13}C$-CO_2 reached −7.8 ‰. Interestingly, the $\delta^{13}C$-DIC of the samples with a pH below 6.00 and alkalinity below 1.00 mmol/L did not increase with decreasing pH. Under the condition of low DIC concentration and low pH, the physical and chemical processes that affect carbon isotope fractionation in natural water no longer play a leading role. The microbial degradation and mineralization of dissolved organic carbon under oligotrophic acidic conditions should be the reason for this phenomenon (Atekwana and Fonyuy, 2009).

4.2. Non-coevolution of DIC concentration and alkalinity

In weakly alkaline water, DIC and alkalinity often follow the law of coevolution. Chou et al. (2017), Jiang et al. (2013) and Li et al. (2017) discovered the non-coevolution phenomenon by calculating ΔDIC1 and ΔTA (Fig. 7(a)): Terrestrial and sewage input is a major reason for the evolution of ΔTA:ΔDIC1 along a 1:1 ratio in the offshore area of Jiaozhou Bay; the dissolution and precipitation of carbonate minerals will impel ΔTA:ΔDIC1 to trend toward 2:1; and biological processes,

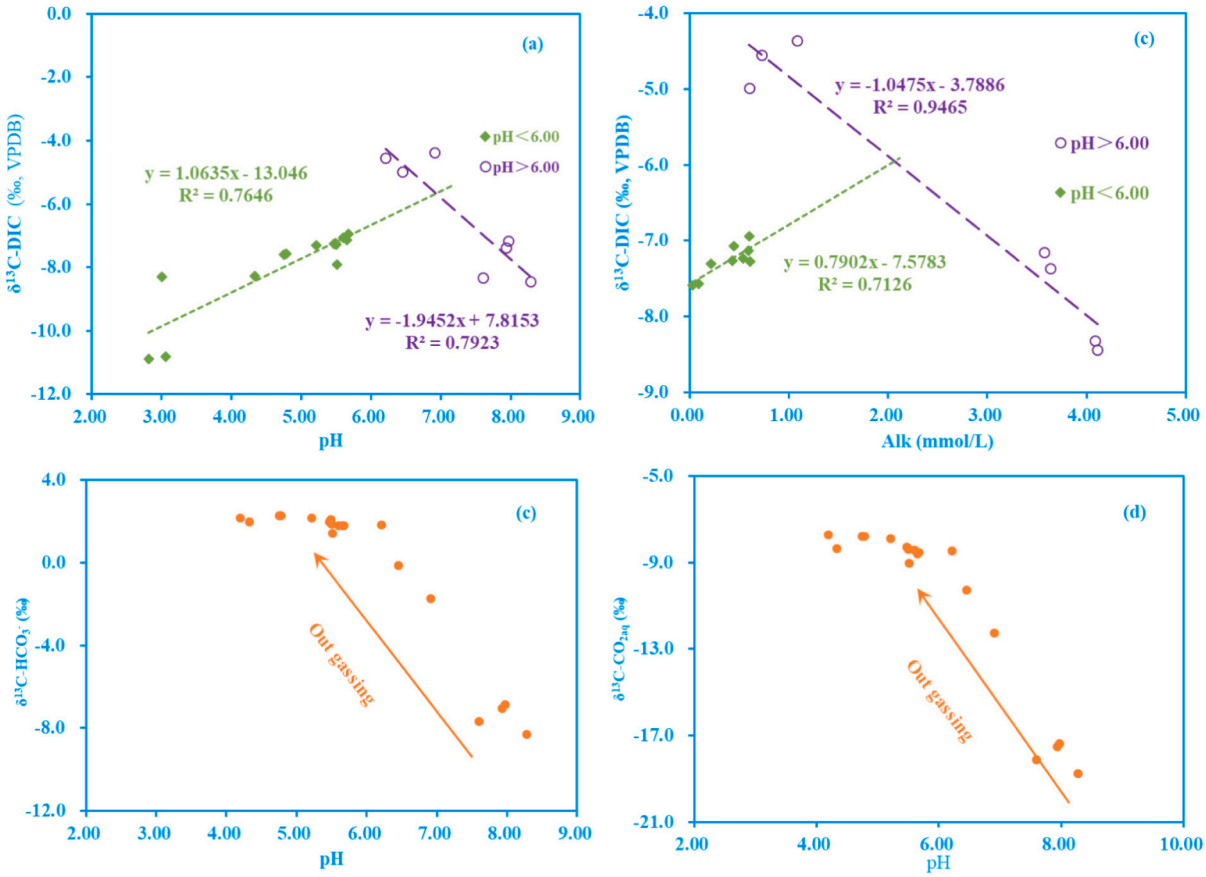

Fig. 6. Dynamic transformation of DIC component concentration and isotope driven by pH (data from January 2021).

such as photosynthesis and respiration (organic matter mineralization), alter DIC and TA in a ratio of 106:15. In this study, the erosion effect of AMD will also cause salinity to increase. Additionally, salinity correlates closely to TA and HCO_3^- (Fig. S4). Therefore, we attempted to use a similar method to explain the non-coevolution of DIC and TA in the Chetian River.

Obviously, the entire Chetian River is currently experiencing significant CO_2 degassing due to the input of AMD with low pH (Fig. 7(a)). Considering the low pH values of W4-4-1 to W10 and the fact that the Chetian River is generally in a karst geological setting, the carbonate dissolution induced by H_2CO_3 should be conditional. In spring, the carbonate dissolution induced by H_2SO_4 and organic mineralization induces a significant increase in DIC supplementation and insignificant TA variation (arrow direction of DOM mineralization; Li et al., 2017). Similar to the Huatan River (Huang et al., 2022), the data points falling in the trend toward 1:1 in the first quadrant represent the coevolution of the DIC concentration and alkalinity in the river section from W2 to W4-4. According to the saturation index of calcite (Table S1), a precipitation of calcite is evident in the reach spanning from W2 to W4-4; however, this process is not clearly shown in Fig. 7(a), indicating that this phenomenon is not a dominant carbon cycle process in the watershed.

To reveal the major processes affecting $\delta^{13}C\text{-}HCO_3^-$ evolution, we drew from the ideas of Alling et al. (2012), Samanta et al. (2015), and Wang et al. (2019). Our consideration of these concepts, together with the data in Table S1, led to the establishment of a DIC evolution model based on ΔDIC2 and $\Delta\delta^{13}C$-DIC.

Organic matter degradation and respiration will lead to an increase in DIC content and the lightening of $\delta^{13}C$-DIC. Thus, this process is connected to the negative correlation between ΔDIC2 and $\Delta\delta^{13}C$-DIC (Fig. 6(b); De Montety et al., 2011; Alling et al., 2012; Wang et al., 2019; Li et al., 2024). Notably, the low pH in the Chetian River makes the water unsuitable for establishing an aquatic ecosystem, while the watershed also features strong hydrodynamic conditions; thus, aquatic ecological processes such as respiration are not the main factors affecting the evolution of DIC. As can be clearly observed, the data points in the fourth quadrant in Fig. 6(b) mainly reflect the mineralization of organic matter and the subsequent dissolution of carbonate rocks (Carbonate Dissolution Pathway II). In addition, the Permian and Triassic coal-bearing strata in the Chetian River are extensively exposed and host multiple coal mines (Fig. 1). After the leaching of coal-bearing strata and gangue, the degradation of sedimentary organic matter may also represent a potential source of DIC. Accordingly, this possibility highlights the need to conduct a further quantitative study on the source of organic matter in the basin.

The precipitation of carbonate does not appear to be the primary factor controlling DIC evolution in the Chetian River under the influence of AMD, as can be discerned from Fig. 6(b). Correspondingly, indications pointing to the dissolution of carbonate should have been relatively obvious. However, Fig. 6(b) does not seem to reflect this process clearly (Carbonate Dissolution Pathway I). We believe that under a low-pH condition, the DIC component immediately participates in the degassing process, leading to the failure of ΔDIC2 to reflect the carbonate dissolution. As another karst erosion process that requires consideration, the degradation of organic carbon actually produces a certain amount of acidity that, in turn, corrodes a certain amount of carbonate rock (Samanta et al., 2015). As illustrated in Fig. 6(b), Carbonate Dissolution Pathway II significantly increases the DIC concentration, while the $\delta^{13}C$-DIC reflects the mixing effect of both organic and carbonate carbon pools.

Both photosynthesis and CO_2 degassing can result in a decreased DIC

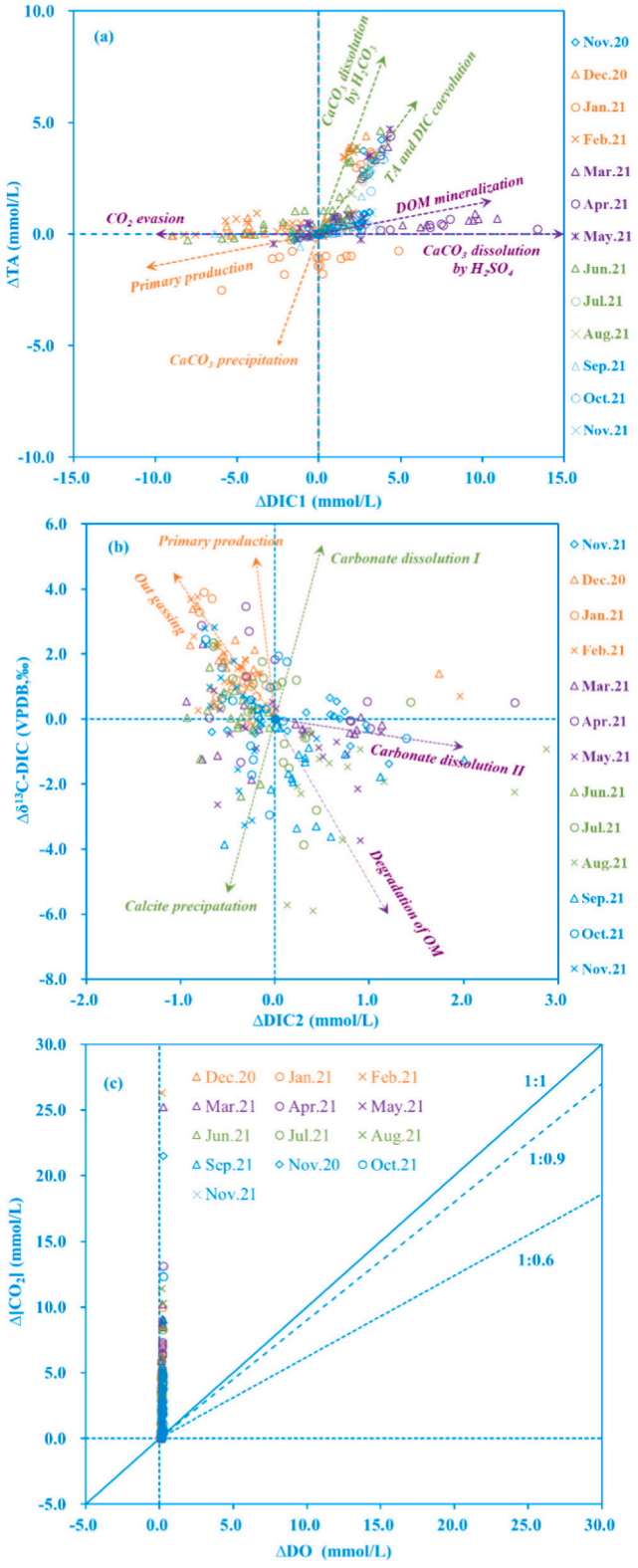

Fig. 7. (a) Correlation diagram of ΔDIC1 and ΔTA in the Chetian River Basin; (b) correlation between salinity of $\Delta\delta^{13}$C-DIC and ΔDIC2 in the Chetian River Basin, and (c) correlation diagram of ΔCO_2 and ΔDO in the Chetian River Basin.

concentration and an increase in δ^{13}C-DIC. These similar consequences make distinguishing between the two processes difficult (Samanta et al., 2015; Wang et al., 2019). The low pH in the Chetian River is not conducive to establishing an aquatic ecosystem, precluding photosynthesis as the main cause of a decrease in DIC concentration and increase in δ^{13}C-DIC (Fig. 6(b)). Based on the analysis in Section 4.1, the main replenishment source of river water in the Chetian River in winter comes from AMD generated during coal mining, causing the river's pH to be relatively low during that season. Hence, the CO_2 degassing process in Fig. 6(b) mainly reflects the situation in reaches from W4-4-1 to W8 under the influence of AMD input.

4.3. Carbonate dissolution and CO_2 degassing characteristics

According to Zhai et al. (2005) and Wang et al. (2015), a dynamic equilibrium exists between the DO and water-soluble CO_2 in freshwater systems (Fig. 7(c)). When the $\Delta CO_2/\Delta DO$ is between 0.62 and 0.97, aquatic respiration and photosynthesis control the dynamic balance of the CO_2 and O_2. When it is below 0.62, the consumption of DO does not produce a corresponding excess of CO_2. When the $\Delta CO_2/\Delta DO$ is >1.0, the excess CO_2 is primarily the result of water acidification and the dissolution of carbonate rocks. As Fig. 7(c) illustrates, the contribution of $\Delta CO_2/\Delta DO$ in the Chetian River is nearly parallel to the vertical axis, confirming that excess protons are the principal cause of excess CO_2. In Fig. S5, the measured pH decreased gradually as the ΔDO increased. At the same time, the DIC levels began to rise. This phenomenon may reflect the loss of DO from its being used to oxidize Fe^{2+} and other metal-reducing ions at the beginning, followed by a low enough pH to support the rapid dissolution of carbonate rocks.

Fig. 8(a) demonstrates the equilibrium relationship of $[2 \times (Ca^{2+}+Mg^{2+})]$ versus $[HCO_3^- + 2 \times SO_4^{2-}]$, revealing the process of H_2SO_4 dissolving limestone. The excessive H_2SO_4 indicates that this process has not yet reached equilibrium; thus, further dissolution of the limestone is still needed. The data points in Fig. 8(b) happen to fall on the evolution line, with a ratio of $[H^+ + 2 \times (Ca^{2+}+Mg^{2+})]$ to $[HCO_3^- + 2 \times SO_4^{2-}]$ of 1:1, further confirming this speculation. The coevolution of $[2 \times (Ca^{2+}+Mg^{2+})]$ and $[HCO_3^-]$ indicates that the buffering of the carbonate system in the water during the initial addition of H_2SO_4 results in the production of a large amount of free CO_2 (Fig. 8(c)). In this section of the river (W2 to W4-4), CO_2 drives the dissolution of limestone; however, the CO_2 degassing rate is much higher than the dissolution rate of limestone (the average pCO_2 decreased from 11,307 μatm at sampling point W2 to 5317 μatm at W4-4). With the continuous addition of H_2SO_4, when the amount of $[H^+]$ exceeds the buffer capacity of the river carbonate system, the dissolution of limestone is transformed from a CO_2-driven into a proton-driven process (Fig. 8(d)), which leads to a further increase in the dissolution rate of carbonate rocks and in the CO_2 degassing rate.

According to Wicks and Groves (1993), under varying pH conditions, carbonate dissolution is controlled by three mechanisms: H^+ drive, H_2CO_3* dissolution, and water molecular dissolution. Atekwana and Fonyuy (2009) thought that the AMD-driven CO_2 degassing of surface water could be summarized as comprising two processes: proton driving and neutralization buffering. According to the pH variation and CO_2 degassing characteristics in different river sections, the Chetian River can be divided into 3 reaches (Fig. 9). The first reach (W2 to W4-4) is mainly characterized by hydrodynamic diffusion degassing in source streams (Yan et al., 2020). In this reach, the pH rose from 7.60 to 7.97, which was driven by CO_2 degassing. The pH of the second reach could be as low as 3.19. This reach (W4-4-4 to W8) is dominated by proton-enhanced degassing. Due to the CO_2 degassing that is directly driven by H^+, the DIC concentration in this reach is not high. In this case, the carbon isotope exchange at the air-water interface makes the δ^{13}C-DIC lighter than −10.0 ‰. In this reach, the erosion of carbonate could also be driven by carbonic acid produced by organic matter mineralization. The third reach (W10 to W11) is dominated by HCO_3^--neutralized degassing. In this section, the pH was between 5.0 and 6.0, and the input of domestic sewage and the mineralization of organic matter contributed some DIC to the river water.

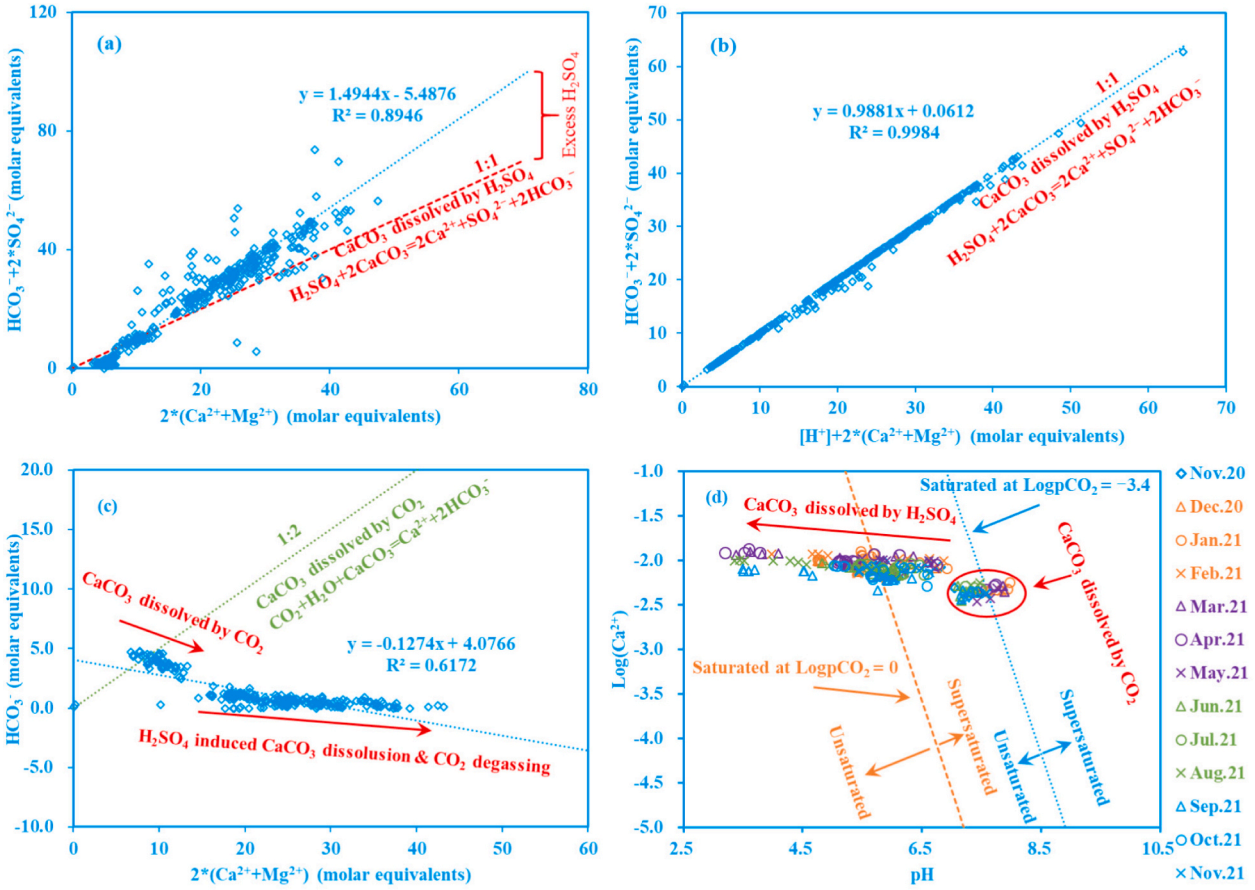

Fig. 8. (a) Correlation diagram of $2 \times (Ca^{2+}+Mg^{2+})$ and $HCO_3^- + 2 \times SO_4^{2-}$; (b) correlation diagram of $H^+ + 2 \times (Ca^{2+}+Mg^{2+})$ and $HCO_3^- + 2 \times SO_4^{2-}$; (c) correlation diagram of $2 \times (Ca^{2+}+Mg^{2+})$ and HCO_3^-; (d) correlation diagram of $Log(Ca^{2+})$ and pH.

4.4. CO_2 degassing scale and the buffering effect

The degassing scale was estimated by calculating the pCO_2 and F-CO_2 (Tables S2 and S3). Compared to typical rivers worldwide, such as the Hudson, the Ottawa, the Mississippi, the Amazon, the Yangtze, the Wujiang, and the Guijiang (Zhang et al., 2019), the pCO_2 in the Chetian River under the influence of AMD was found to be 1 to 2 orders of magnitude higher (Table S4). The highest F-CO_2 was up to 498.3 g C m^{-2} d^{-1}. At the confluence of the Chetian and Huatan rivers (HT9), this value was only 1.8 g C m^{-2} d^{-1}, while the unaffected upstream (HT9-1) had an even lower F-CO_2 of 1.0 g C m^{-2} d^{-1}. In terms of seasonal changes, the F-CO_2 was significantly lower in winter and spring than in summer and autumn (Fig. 4). The corresponding CO_2 emissions from the entire Chetian River totaled 217,144.0 kg during this study (Table S5).

In karst medium-high sulfur coal mining areas, the dissolution of carbonate rocks activates the old carbon fixed in the strata, thereby increasing the ability of water bodies in the basin to release CO_2 into the atmosphere. Conversely, the dissolution of carbonate rocks consumes the acidity of the surface water, which may also weaken the F-CO_2 released from the surface water into the atmosphere. Overall, the monthly CO_2 degassing level in the Chetian River accounts for 10.3 % to 62.3 % of the total DIC in water, with an average of only 23.0 % throughout the year. This degassing level is much lower than the estimates of Hercod et al. (1998) and Fonyuy and Atekwana (2008). The degassing loss of DIC is related to the quantity of AMD input and the content of bicarbonate in the water. In karst areas, the erosion of sufficient carbonate rocks consumes the acidity in the surface water, resulting in a lower degassing ratio than that in non-carbonate rock areas.

The thin boundary layer method is commonly used to estimate CO_2 emissions from oceans and natural freshwater. However, further evaluation is needed for its applicability in acidic water. The mass balance of upstream and downstream DIC can be used to estimate the CO_2 degassing scale in AMD-affected rivers (Vesper et al., 2016). However, processes such as DIC replenishment from different sources and the dilution of rainwater can bring some uncertainty. Especially in low pH condition, it is insufficient to only consider the potential acidity generated by metal ion hydrolysis while ignoring the acidity of protons, as shown in Fig. 8(a) and (b). Atekwana and Fonyuy (2009) provided measured pCO_2 data, and the F-CO_2 based on the measured pCO_2 was basically consistent with the calculation of the thin boundary layer method when the pH of the water sample is >7.0. However, the results of the two methods differ by up to 4–5 orders of magnitude when the pH < 4.5. Under low pH and high pCO_2 conditions, the CO_2 degassing rate is very fast. Hence, the measured DIC concentration and pCO_2 will be much lower than the theoretical level, resulting in a significantly lower estimated F-CO_2. We even believe that the acidity in water still has the potential to further dissolve carbonate rocks under low pH conditions. This part of CO_2 is not reflected in the thin boundary layer method, which makes the F-CO_2 result underestimated.

In addition, the Huatan River drains a karst region, which has a significant buffering effect on the acidity in the Chetian River. The pCO_2 and F-CO_2 decreased rapidly downstream of the confluence of the Chetian and Huatan rivers (Fig. 4). Using the pCO_2 at HT9-1 as a reference, if the pCO_2 of the river water at W11 drops to the same level as HT9-1, approximately 0.56 to 3.36 mmol/L of DIC would be released into the atmosphere as CO_2 (Table S6). In other words, from November 2020 to November 2021, the buffering effect of the river water in HT9

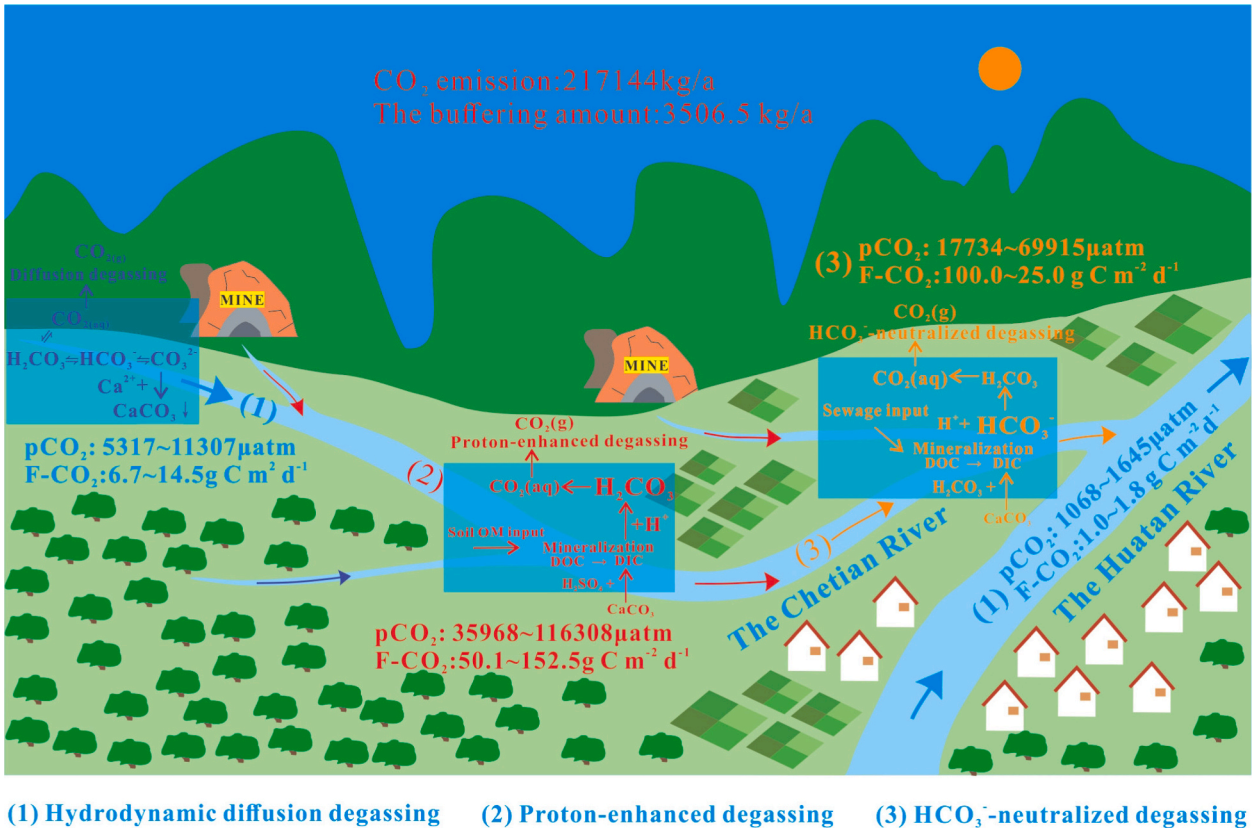

Fig. 9. Conceptual model of DIC evolution in different river sections.

against the water in W11 avoided the release of about 3506.5 kg of additional CO_2. The buffering percentage was approximately 74.1 % to 97.4 % of the DIC concentration at point W11. It should be noted that this estimation is only approximate. In the future, a more scientific assessment needs to be conducted in conjunction with direct observations.

5. Conclusion

(1) Precipitation has a significant impact on the carbon emission effect of AMD. In winter, atmospheric precipitation is relatively scarce, and the main supply for the Chetian River is AMD generated during coal mining, resulting in a relatively low pH value in the river. In summer, the dilution effect of a large amount of atmospheric precipitation during the rainy season leads to increased pH values in the river. The seasonal variations in pH affect the dynamic transformation of different DIC components and CO_2 degassing.

(2) Based on the non-coevolution of DIC and alkalinity, as well as the analysis results concerning ΔDIC and $\Delta\delta^{13}$C-DIC, the dissolution of carbonate, organic matter degradation, and domestic sewage input contributed varying degrees of DIC to this river. The stoichiometric balance of $\Delta[CO_2]$ and ΔDO suggests that the CO_2 excess was mainly driven by the input of low-pH AMD.

(3) HCO_3^--neutralized degassing and proton-enhanced degassing are the main CO_2 degassing processes in the Chetian River. The average pCO_2 in the Chetian River decreased along the flow direction significantly from 116,308 μatm to 17,734 μatm, with a total of 217,144.0 kg of CO_2 released from November 2020 to November 2021. Overall, the CO_2 degassing level in the Chetian River accounts for 10.3 % to 62.3 % of the total DIC in the water, with an average of 23.0 % throughout the year.

(4) In karst areas, the erosion of sufficient carbonate rocks neutralizes the acidity in surface water, resulting in a lower degassing ratio than that in non-carbonate rock areas. The buffering effect of the Huatan River on the AMD-affected river water in the Chetian River avoids the release of about 3506.5 kg of CO_2 from November 2020 to November 2021, accounting for approximately 85.2 % of the total DIC output at the outlet.

CRediT authorship contribution statement

Qingguang Li: Conceived and designed the analysis, Performed the analysis, Wrote the paper
Pan Wu: Conceived and designed the analysis, Manuscript correction
Shilu Wang: Conceived and designed the analysis, Manuscript correction
Jiangxun Huang, Sample collection, Performed the analysis
Weiqi Lu: Sample collection, Manuscript correction
Di Tan: Experimental tests, Manuscript correction
Shangyi Gu: Experimental test, Manuscript correction
Bailing Fan: Manuscript correction.

Declaration of competing interest

The authors declare that they have no known competing financial interests or personal relationships that could have appeared to influence the work reported in this paper.

Data availability

Data will be made available on request.

Acknowledgement

This study was sponsored by the National Natural Science Foundation of China (Nos. 41867050, 42267033), the Guizhou Provincial Science and Technology Foundation ([2019]1155), the National Key Research and Development Program of China (No. 2019YFC1805300), and the Post subsidy funds corresponding to this National Key Research and Development Program of China.

Appendix A. Supplementary data

Supplementary data to this article can be found online at https://doi.org/10.1016/j.scitotenv.2023.165856.

References

Alin, S.R., de Fátima, F.L., Rasera, M., Salimon, C.I., Richey, J.E., Holtgrieve, G.W., Krusche, A.V., Snidvongs, A., 2011. Physical controls on carbon dioxide transfer velocity and flux in low-gradient river systems and implications for regional carbon budgets. J. Geophys. Res. Biogeosci. 116 (G1), 1–17.

Alling, V., Porcelli, D., Mörth, C.M., Anderson, L.G., Sanchez-Garcia, L., Gustafsson, Ö., Andersson, P.S., Humborg, C., 2012. Degradation of terrestrial organic carbon, primary production and out-gassing of CO_2 in the Laptev and East Siberian Seas as inferred from $\delta^{13}C$ values of DIC. Geochim. Cosmochim. Acta 95, 143–159.

Atekwana, E.A., Fonyuy, E.W., 2009. Dissolved inorganic carbon concentrations and stable carbon isotope ratios in streams polluted by variable amounts of acid mine drainage. J. Hydrol. 372 (1), 136–148.

Balci, N., Demirel, C., 2018. Prediction of acid mine drainage (AMD) and metal release sources at the Küre Copper Mine Site, Kastamonu, NW Turkey. Mine Water Environ. 37 (1), 56–74.

Cai, W.J., Wang, Y., 1998. The chemistry, fluxes, and sources of carbon dioxide in the estuarine waters of the satilla and altamaha rivers, georgia. Limnol. Oceanogr. 43 (4), 657–668.

Cai, W.J., Guo, X., Chen, C.T.A., Dai, M., Zhang, L., Zhai, W., Lohrenz, S.E., Yin, K., Harrison, P.J., Wang, Y., 2008. A comparative overview of weathering intensity and HCO_3^- flux in the world's major rivers with emphasis on the Changjiang, Huanghe, Zhujiang (Pearl) and Mississippi Rivers. Cont. Shelf Res. 28 (12), 1538–1549.

Chen, Y., Zhu, S., Yang, C., Xiao, S., 2021. Analysis of hydrochemical evolution in main discharge aquifers under mining disturbance and water source identification. Environ. Sci. Pollut. Res. 28 (21), 26784–26793.

Chou, W.C., Tishchenko, P.Y., Chuang, K.Y., Gong, G.C., Shkirnikova, E.M., Tishchenko, P.P., 2017. The contrasting behaviors of CO_2 systems in river-dominated and ocean-dominated continental shelves: a case study in the East China Sea and the Peter the Great Bay of the Japan/East Sea in summer 2014. Mar. Chem. 195, 50–60.

Clark, J.F., Wanninkhof, R.I.K., Schlosser, P., Simpson, H.J., 1994. Gas exchange rates in the tidal Hudson River using a dual tracer technique. Tellus Ser. B Chem. Phys. Meteorol. 46 (4), 274–285.

De Montety, V., Martin, J.B., Cohen, M.J., Foster, C., Kurz, M.J., 2011. Influence of diel biogeochemical cycles on carbonate equilibrium in a karst river. Chem. Geol. 283 (1–2), 31–43.

Feng, Q., Li, T., Qian, B., Zhou, L., Gao, B., Yuan, T., 2014. Chemical characteristics and utilization of coal mine drainage in China. Mine Water Environ. 33 (3), 276–286.

Fonyuy, E.W., Atekwana, E.A., 2008. Effects of acid mine drainage on dissolved inorganic carbon and stable carbon isotopes in receiving streams. Appl. Geochem. 23 (4), 743–764.

Golding, S.D., Boreham, C.J., Esterle, J.S., 2013. Stable isotope geochemistry of coal bed and shale gas and related production waters: a review. Int. J. Coal Geol. 120, 24–40.

Grande, J.A., De La Torre, M.L., Santisteban, M., Valente, T., Fernandez, J.P., Pérez-Ostalé, E., 2016. Spatial evolution of an AMD stream in the Iberian Pyrite Belt: process characterization and control factors on the hydrochemistry. Hydrol. Sci. J. 61 (8), 1503–1511.

Gu, D.Z., Li, J.F., Cao, Z.G., Wu, B.Y., Jiang, B.B., Yang, Y., Yang, J., Chen., Y.P., 2021. Technology and engineering development strategy of water protection and utilization of coal mine in China. J. China Coal Soc. 46 (10), 3079–3089.

Hercod, D.J., Brady, P.V., Gregory, R.T., 1998. Catchment-scale coupling between pyrite oxidation and calcite weathering. Chem. Geol. 151 (1–4), 259–276.

Huang, Y., Li, Q., 2019. Karst biogeochemistry in China: past, present and future. Environ. Earth Sci. 78 (15), 1–14.

Huang, J., Li, Q., Wu, P., Wang, S., Guo, M., Liu, K., 2022. The effects of weathering of coal-bearing stratum on the transport and transformation of DIC in karst watershed. Sci. Total Environ. 838 (4), 156436.

Jiang, L.Q., Cai, W.J., Wang, Y., Bauer, J.E., 2013. Influence of terrestrial inputs on continental shelf carbon dioxide. Biogeosciences 10 (2), 839–849.

Kruse, N.A., Strosnider, W.H., 2015. Carbon dioxide dynamics and sequestration in mine water and waste. Mine Water Environ. 34 (1), 3–9.

Lemay, T.G., 2003. Chemical and Physical Hydrogeology of Coal, Mixed Coal-Sandstone and Sandstone Aquifers From Coal-Bearing Formations in the Alberta Plains Region, Alberta.

Li, Q., Wu, P., 2022. Research progress on the acidification features of coal mine drainage and its carbon emission effect during coal exploitation. Environ. Eng. Manag. J. 21 (12), 1975–1985.

Li, Q., Ju, Y., Lu, W., Wang, G., Neupane, B., Sun, Y., 2016. Water-rock interaction and methanogenesis in formation water in the southeast Huaibei coalfield, China. Mar. Pet. Geol. 77, 435–447.

Li, Y., Yang, X., Han, P., Xue, L., Zhang, L., 2017. Controlling mechanisms of surface partial pressure of CO_2 in Jiaozhou Bay during summer and the influence of heavy rain. J. Mar. Syst. 173, 49–59.

Li, B., Wang, X.Q., Liu, Z.J., Li, T., 2021. Study on multi-field catastrophe evolution laws of water inrush from concealed karst cave in roadway excavation: a case of Jiyuan coal mine. Geomatics Nat. Hazards Risk 12 (1), 222–243.

Li, L., Cao, X., Bu, C., Wu, P., Tian, B., Dai, Y., Ren, Y., 2024. Effects of acid mine drainage on photochemical and biological degradation of dissolved organic matter in karst river water. J. Environ. Sci. https://doi.org/10.1016/j.jes.2022.12.012.

Liu, Z., Dreybrodt, W., Liu, H., 2011. Atmospheric CO_2 sink: silicate weathering or carbonate weathering? Appl. Geochem. 26, S292–S294.

Liu, J.J., Dai, S.F., Song, H.J., Nechaev, V.P., French, D., Spiro, B.F., Granham, I.T., Hower, J.C., Shao, L.Y., Zhao, J.T., 2021. Geological factors controlling variations in the mineralogical and elemental compositions of Late Permian coals from the Zhijin-Nayong Coalfield, western Guizhou, China. Int. J. Coal Geol. 247, 103855.

McIntosh, J.C., Walter, L.M., Martini, A.M., 2002. Pleistocene recharge to midcontinent basins: effects on salinity structure and microbial gas generation. Geochim. Cosmochim. Acta 66 (10), 1681–1700.

Millero, F.J., 2010. Carbonate constants for estuarine waters. Mar. Freshw. Res. 61 (2), 139–142.

Mook, W.G., Bommerson, J.C., Staverman, W.H., 1974. Carbon isotope fractionation between dissolved bicarbonate and gaseous carbon dioxide. Earth Planet. Sci. Lett. 22 (2), 169–176.

Nordstrom, D.K., Blowes, D.W., Ptacek, C.J., 2015. Hydrogeochemistry and microbiology of mine drainage: an update. Appl. Geochem. 57, 3–16.

Pope, J., Newman, N., Craw, D., Trumm, D., Rait, R., 2010. Factors that influence coal mine drainage chemistry West Coast, South Island, New Zealand. N. Z. J. Geol. Geophys. 53 (2–3), 115–128.

Raymond, P.A., Oh, N.H., 2009. Long term changes of chemical weathering products in rivers heavily impacted from acid mine drainage: insights on the impact of coal mining on regional and global carbon and sulfur budgets. Earth Planet. Sci. Lett. 284 (1), 50–56.

Rice, K.C., Herman, J.S., 2012. Acidification of Earth: an assessment across mechanisms and scales. Appl. Geochem. 27 (1), 1–14.

Sağlam, E.S., Akçay, M., Çolak, D.N., Bektaş, K.İ., Beldüz, A.O., 2016. Generation of acid mine drainage around the Karaerik copper mine (Espiye, Giresun, NE Turkey): implications from the bacterial population in the Acısu effluent. Extremophiles 20 (5), 673–685.

Samanta, S., Dalai, T.K., Pattanaik, J.K., Rai, S.K., Mazumdar, A., 2015. Dissolved inorganic carbon (DIC) and its $\delta^{13}C$ in the Ganga (Hooghly) River estuary, India: evidence of DIC generation via organic carbon degradation and carbonate dissolution. Geochim. Cosmochim. Acta 165, 226–248.

Sasowsky, I.D., White, W.B., 1993. Geochemistry of the Obey River Basin, north-central Tennessee: a case of acid mine water in a karst drainage system. J. Hydrol. 146, 29–48.

Singer, P.C., Stumm, W., 1970. Acidic mine drainage: the rate-determining step. Science 167 (3921), 1121–1123.

Strosnider, W.H.J., López, F.L., LaBar, J.A., Palmer, K.J., Nairn, R.W., 2014. Unabated acid mine drainage from Cerro Rico de Potosí, Bolivia: uncommon constituents of concern impact the Rio Pilcomayo headwaters. Environ. Earth Sci. 71 (7), 3223–3234.

Sun, W., Wu, Q., Dong, D., Jiao, J., 2012. Avoiding coal-water conflicts during the development of China's large coal-producing regions. Mine Water Environ. 31, 74–78.

Sun, Y.J., Chen, G., Xu, Z., M., 2020. Research progress of water environment, treatment and utilization in coal mining areas of China. J. China Coal Soc. 45 (1), 304–316.

Tan, D., Li, Q., Wang, S., Yeager, K.M., Guo, M., Liu, K., Wang, Y., 2021. Diel variation of CH_4 emission fluxes in a small artificial lake: toward more accurate methods of observation. Sci. Total Environ. 784, 147146.

Tang, Y.G., Sun, Y.W., Wang, X.S., Yan, L.L., Shi, Q., Ni, H.X., Li, W.W., Li, X.L., Finkelman, R.B., Pang, X.P., 2020. Composition and structure of the sulfur-containing compounds in the extracts from the Chinese high-organic-sulfur coals. Energy Fuel 34 (9), 10666–10675.

Tao, X., Wu, P., Tang, C., Liu, H., Sun, J., 2012. Effect of acid mine drainage on a karst basin: a case study on the high-As coal mining area in Guizhou province, China. Environ. Earth Sci. 65 (3), 631–638.

Vesper, D.J., Edenborn, H.M., 2012. Determination of free CO_2 in emergent groundwaters using a commercial beverage carbonation meter. J. Hydrol. 438, 148–155.

Vesper, D.J., Moore, J.E., Adams, J.P., 2016. Inorganic carbon dynamics and CO_2 flux associated with coal-mine drainage sites in Blythedale PA and Lambert WV, USA. Environ. Earth Sci. 75 (4), 1–14.

Vörös, D., Řimnáčová, D., Medvecká, L., Geršlová, E., Díaz-Somoano, M., 2021. The impact of saline mine water on fate of mineral elements and organic matter: the case study of the Upper Silesian Coal Basin. Chemosphere 284, 131397.

Wang, S., Yeager, K.M., Wan, G., Liu, C.Q., Liu, F., Lü, Y., 2015. Dynamics of CO_2 in a karst catchment in the southwestern plateau, China. Environ. Earth Sci. 73 (5), 2415–2427.

Wang, W., Li, S.L., Zhong, J., Li, C., Yi, Y., Chen, S., Ren, Y., 2019. Understanding transport and transformation of dissolved inorganic carbon (DIC) in the reservoir system using $\delta^{13}C_{DIC}$ and water chemistry. J. Hydrol. 574, 193–201.

Wanninkhof, R., 1992. Relationship between wind speed and gas exchange over the ocean. J. Geophys. Res. Oceans 97 (C5), 7373–7382.

Wanninkhof, R., 2014. Relationship between wind speed and gas exchange over the ocean revisited. Limnol. Oceanogr. Methods 12 (6), 351–362.
Weisener, C.G., Weber, P.A., 2010. Preferential oxidation of pyrite as a function of morphology and relict texture. N. Z. J. Geol. Geophys. 53 (2–3), 167–176.
Wicks, C.M., Groves, C.G., 1993. Acidic mine drainage in carbonate terrains: geochemical processes and rates of calcite dissolution. J. Hydrol. 146, 13–27.
Wolf-Gladrow, D.A., Zeebe, R.E., Klaas, C., Körtzinger, A., Dickson, A.G., 2007. Total alkalinity: the explicit conservative expression and its application to biogeochemical processes. Mar. Chem. 106 (1–2), 287–300.
Wu, Qiang, 2014. Progress, problems and prospects of prevention and control technology of mine water and reutilization in China. J. China Coal Soc. 39 (5), 795–805.
Yan, H., Liu, Z., Sun, H., 2020. Large degrees of carbon isotope disequilibrium during precipitation-associated degassing of CO2 in a mountain stream. Geochim. Cosmochim. Acta 273, 244–256.
Zeng, C., Liu, Z.H., Zhao, M., Yang, R., 2016. Hydrologically-driven variation in karst process-related carbon sink flux: insights from high-resolution monitoring of three typical karst catchments in the subtropical karst area of SW China. J. Hydrol. 533, 74–90.
Zhai, W., Dai, M., Cai, W.J., Wang, Y., Wang, Z., 2005. High partial pressure of CO_2 and its maintaining mechanism in a subtropical estuary: the Pearl River estuary, China. Mar. Chem. 93 (1), 21–32.
Zhang, T., Li, J., Pu, J., Yuan, D., 2019. Carbon dioxide exchanges and their controlling factors in Guijiang River, SW China. J. Hydrol. 578, 124073.
Zhang, R., Wu, P., Ye, H., Li, X., 2021. Hydrogeochemical characteristics and quality assessment of mine water in coalfield area, Guizhou Province, Southwest China. Bull. Environ. Contam. Toxicol. 107 (6), 1087–1094.